Improved Ising formulation of max-3-cut using higher-order spin interactions

Robbe De Prins,[1,2,*] Guy Van der Sande,[2] Peter Bienstman,[1] and Thomas Van Vaerenbergh[3]

[1] *Photonics Research Group, Ghent University— imec, Technologiepark-Zwijnaarde 126, 9052 Gent, Belgium*

[2] *Applied Physics Research Group, Vrije Universiteit Brussel, Pleinlaan 2, 1050 Brussels, Belgium*

[3] *Large-Scale Integrated Photonics Lab, Hewlett Packard Labs, HPE Belgium, Diegem, Belgium*

(Received 5 August 2025; revised 14 January 2026; accepted 27 March 2026; published 21 April 2026)

Many combinatorial optimization problems (COPs) are naturally expressed using variables that take on more than two discrete values. To solve such problems using Ising machines (IMs)—specialized analog or digital devices designed to solve COPs efficiently—these multivalued integers must be encoded using binary spin variables. A common approach is one-hot encoding, where each variable is represented by a group of spins constrained so that exactly one spin is in the "up" state. However, this encoding introduces energy barriers: changing an integer's value requires flipping two spins and passing through an invalid intermediate state. This creates rugged energy landscapes that may hinder optimization. We propose a higher-order Ising formulation for max-3-cut, a canonical COP involving integers with three possible states that provides a minimal setting for assessing multivalued formulations on IMs. Our formulation preserves valid configurations under single-spin updates. The resulting energy landscapes are smoother, and we show that this remains true even when the binary variables are relaxed to continuous values, making it well suited for analog IMs as well. Benchmarking on such an IM, we find that the higher-order formulation leads to higher success rates and faster time-to-solution than when one-hot encoding is employed.

DOI: 10.1103/vqsv-jzk4

I. INTRODUCTION

The challenge of solving a combinatorial optimization problem (COP) can be formulated as the task of finding the global minimum of an energy landscape. Many COPs are naturally expressed using *multivalued integer variables*, that is to say, variables that can take one of K discrete states. Examples can be found in statistical physics [1,2], biology [3,4], gas and power networks [5], data clustering [6], scheduling [7,8], and elsewhere [9,10]. Although hardware solvers that directly use multivalued variables have been proposed, such as Potts machines [11, 12], most research focuses on binary-variable hardware, such as Ising machines (IMs) [13–17], adiabatic quantum computing [18], and variational quantum approaches [19,20]. This focus stems from the fact that any COP can be reformulated as an Ising problem or, alternatively, as a quadratic unconstrained binary optimization (QUBO) problem, using only a polynomial overhead [21].

To represent multivalued integer variables within IMs, a common approach is *one-hot encoding*, where each K-state variable is represented by K spins. For each state $i \in \{1, \ldots, K\}$, the corresponding spin configuration has the ith spin set to 1 and all remaining spins are set to -1. In the case of a single isolated K-state variable, the Ising energy landscape is designed such that each of the K one-hot configurations—corresponding to one valid state of the multivalued integer—has the same minimal energy, while all other (invalid) configurations have a higher energy. Importantly, transitioning between valid states requires flipping two spins, and if these flips are performed sequentially, the system must pass through an invalid intermediate state. As a result, valid states are separated by energy barriers, creating a rugged landscape that complicates finding the global energy minimum and solving the COP.

In this work, we consider the max-3-cut problem, a variant of graph coloring, and one of the simplest canonical COPs that involves multivalued integer variables. We propose an alternative max-3-cut formulation that utilizes spin variables with higher-order interactions, that is, a higher-order Ising formulation (also known as polynomial unconstrained spin optimization). We will show that this formulation doubles the number of valid configurations while also allowing transitions between logical states via single-spin flips, thereby eliminating energy barriers.

*Contact author: robbe.deprins@ugent.be

Our work is conceptually parallel to insights from recent studies on Boolean satisfiability (SAT) problems, where converting native higher-order formulations into quadratic alternatives was found to introduce similar ruggedness [16,22–24]. Here, we reverse that path—replacing a quadratic formulation with a higher-order one—to recover smoother energy landscapes. Note that our higher-order formulation is otherwise unrelated to SAT problems. For example, whereas quadratization methods for SAT problems introduce auxiliary variables, our max-3-cut formulation preserves the variable count of its quadratic counterpart.

We further demonstrate that the structural benefits of the higher-order max-3-cut formulation persist under continuous relaxations of the spin variables. This setting is relevant for analog IMs, which have attracted increasing attention in recent years [13,15,17,25–31], also motivated by recent work on extensions to continuous vector spins [32,33].

Finally, we benchmark both formulations using an analog IM inspired by simulated bifurcation dynamics [14,34]. The higher-order Ising formulation yields consistently higher success rates and faster operation than the standard Ising formulation. In addition, we investigate an empirical rescaling of the Ising formulation—a heuristic proposed in previous work. Although this rescaling improves the performance of the quadratic formulation, it is still outperformed by our higher-order approach. Moreover, we show that the benefit of this rescaling cannot be fully explained by analyzing the individual components of the quadratic model in isolation, highlighting the importance of empirical parameter tuning in COP encodings. We conclude by outlining future directions to better understand and exploit this behavior.

II. MAX-3-CUT FORMULATIONS

The goal of the max-3-cut problem is to partition the vertices of an undirected graph into three disjoint sets while maximizing the number of edges connecting different sets. This can be viewed as a type of graph coloring, where each vertex is assigned one of three colors—say, red, green, or blue—with the goal of minimizing the number of edges between vertices of the same color.

A. Ising formulation

In Ref. [9], a quadratic formulation of the max-3-cut problem in terms of bit variables (i.e., a QUBO formulation) is proposed as follows. Denote the sets of vertices and edges in a given graph by V and E, respectively. For every vertex $v \in V$, a triplet of binary variables is introduced, $x_{v,c}$ where $c \in \{1,2,3\}$, using one-hot encoding: $x_{v,c}$ equals 1 if vertex v has color c, and 0 otherwise. The QUBO energy function is defined as follows:

$$\mathcal{H}_{\mathrm{QUBO}} = A \sum_{v \in V} \left(1 - \sum_{c=1}^{3} x_{v,c}\right)^2 + B \sum_{(uv) \in E} \sum_{c=1}^{3} x_{u,c} x_{v,c}, \tag{1}$$

where A and B are positive scalars. The first term enforces that all variable triplets are one-hot encoded, since this positive term only vanishes if every triplet contains a single 1 and two 0s, ensuring the vertex colors are well defined. The second term adds an energy penalty for every edge that connects vertices with the same color, aligning with the max-3-cut objective. The ratio B/A determines the relative emphasis on valid color assignments versus cut maximization.

We convert the bit variables $x_{v,c} \in \{0,1\}$ to spin variables $\sigma_{v,c} \in \{-1,1\}$ as follows:

$$x_{v,c} = \frac{\sigma_{v,c} + 1}{2}. \tag{2}$$

This yields the following Ising formulation:

$$\mathcal{H}_{\mathrm{Ising}} = \frac{A}{4} \sum_{v} \sum_{c \neq d} \sigma_{v,c} \sigma_{v,d} + \frac{B}{4} \sum_{(uv) \in E} \sum_{c=1}^{3} \sigma_{u,c} \sigma_{v,c} + \sum_{v} \sum_{c=1}^{3} \left(\frac{A}{2} + \frac{B}{4} \deg(v)\right) \sigma_{v,c}, \tag{3}$$

where $\deg(v)$ denotes the degree of vertex v. In deriving Eq. (3) from Eq. (1), we omitted constant terms that do not affect the energy landscape (see Ref. [35] for details).

The allowed spin configurations, each representing a possible vertex color, are defined as follows:

$$\begin{cases} \uparrow\downarrow\downarrow \equiv \text{ red}, \\ \downarrow\uparrow\downarrow \equiv \text{ green}, \\ \downarrow\downarrow\uparrow \equiv \text{ blue}. \end{cases} \tag{4}$$

Note that the remaining (invalid) spin configurations occupy 62.5% of the configuration space. Moreover, transitioning from one valid state to another requires two spin flips, thereby passing through an invalid intermediate state ($\downarrow\downarrow\downarrow$, $\downarrow\uparrow\uparrow$, $\uparrow\downarrow\uparrow$, or $\uparrow\uparrow\downarrow$) that forms an energy barrier.

B. Higher-order Ising formulation

We now propose an alternative max-3-cut formulation using higher-order spin interactions:

$$\mathcal{H}_{\mathrm{HO}} = A \sum_{v} \sum_{c \neq d} \sigma_{v,c}\, \sigma_{v,d} + B \sum_{(uv) \in E} \sum_{c \neq d} \sigma_{u,c}\, \sigma_{v,c}\, \sigma_{u,d}\, \sigma_{v,d}. \tag{5}$$

Moreover, we increase the set of allowed configurations as follows:

$$\begin{cases} \uparrow\downarrow\downarrow \equiv \downarrow\uparrow\uparrow \equiv \text{ red}, \\ \downarrow\uparrow\downarrow \equiv \uparrow\downarrow\uparrow \equiv \text{ green}, \\ \downarrow\downarrow\uparrow \equiv \uparrow\uparrow\downarrow \equiv \text{ blue}. \end{cases} \tag{6}$$

That is, spin triplets now follow one-hot encoding, modulo global spin inversion within each triplet.

It is easy to check that the first term of Eq. (5) stabilizes these states. Indeed, when evaluated on a single spin triplet, this term has a value of $-2A$ for all of the allowed states, while the invalid states $\uparrow\uparrow\uparrow$ and $\downarrow\downarrow\downarrow$ lead to a value of $6A$. The second term of Eq. (5) reflects the max-3-cut objective. Indeed, when considering two connected vertices, it evaluates to $6B$ if the vertices have the same color, while it equals $-2B$ if those vertices have a different color.

Note that Eq. (6) excludes only the $\uparrow\uparrow\uparrow$ and $\downarrow\downarrow\downarrow$ configurations, so invalid states occupy just 25% of the configuration space. Moreover, transitions between any two colors can be achieved with a single-spin flip, thereby avoiding the energy barriers introduced by one-hot encoding in the Ising mapping.

C. Rescaled Ising formulation

Alongside the Ising formulation of Eq. (3), we also consider a simple variant obtained by scaling the terms that are linear in the spin variables by a factor of 0.6:

$$\mathcal{H}_{\text{Ising, res}} = \frac{A}{4}\sum_{v}\sum_{c\neq d}\sigma_{v,c}\sigma_{v,d} + \frac{B}{4}\sum_{(uv)\in E}\sum_{c=1}^{3}\sigma_{u,c}\sigma_{v,c} + 0.6\sum_{v}\sum_{c=1}^{3}\left(\frac{A}{2}+\frac{B}{4}\deg(v)\right)\sigma_{v,c}. \tag{7}$$

This rescaling was first proposed in Ref. [36], which found it to be beneficial for a structure-based drug design problem whose mapping contains one-hot encoding constraints, similar to Eq. (3), along with problem-specific constraints (see Eqs. (5)–(6) and Fig. 3 in Ref. [36]). In our earlier work [35], we showed that the same rescaling is also effective for max-3-cut (see Fig. 5 in Ref. [35]).

At first sight, one would expect this rescaling to distort the intended constraint structure of Eq. (1), causing the one-hot encoding constraint (proportional to A) and the edge-coloring constraint (proportional to B) to be enforced incorrectly. However, our previous results show that this does not occur. Instead, the rescaling improves robustness: it widens the range of B/A values for which the ground state of the formulation corresponds to the correct max-3-cut solution (see Fig. 6 in Ref. [35]).

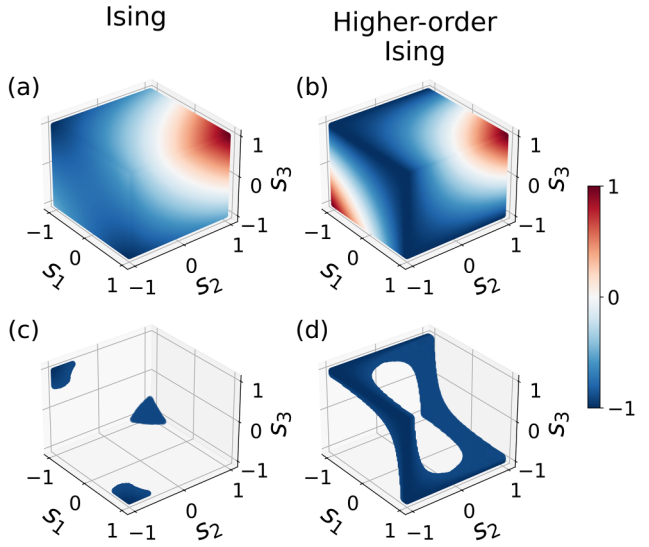

FIG. 1. Normalized energy landscapes for a single vertex, represented by a spin triplet, under the (a) Ising and (b) higher-order Ising formulations. Panels (c) and (d) highlight states with energy below –0.9 for these respective formulations. For the Ising formulation, the lowest-energy states ($\uparrow\downarrow\downarrow$, $\downarrow\uparrow\downarrow$, $\downarrow\downarrow\uparrow$) are separated by energy barriers. In contrast, the minimal energy states for the higher-order Ising formulation ($\uparrow\downarrow\downarrow$, $\downarrow\uparrow\downarrow$, $\downarrow\downarrow\uparrow$, $\downarrow\uparrow\uparrow$, $\uparrow\downarrow\uparrow$, $\uparrow\uparrow\downarrow$) are connected by a flat, barrier-free energy path.

III. ENERGY LANDSCAPES FOR ANALOG SPINS

As discussed above, the higher-order Ising formulation offers clear advantages over the quadratic Ising formulation when working with binary spin variables $\sigma_{v,c} \in \{-1, 1\}$. Unlike the quadratic formulation, which excludes more than half of the configuration space and introduces energy barriers between feasible states, the higher-order formulation permits twice the number of configurations and smoother transitions via single-spin flips, resulting in a less rugged energy landscape. In this section, we extend this comparison to the analog case by replacing binary spins $\sigma_{v,c}$ with continuous variables $s_{v,c} \in \mathbb{R}$. This relaxation is relevant in many combinatorial optimization solvers [13,15,17,25–31].

To illustrate differences in energy landscapes, we visualize small-scale instances of the higher-order Ising formulation of Eq. (5) and the Ising formulation of Eq. (3). As detailed in Appendix C, the rescaled Ising formulation of Eq. (7) produces landscapes similar to the original Ising formulation for these instances. We therefore focus here on comparing the higher-order formulation to the standard quadratic formulation. Visualizations for the rescaled case are provided in Appendix C.

Figures 1(a) and 1(b) visualize the quadratic and higher-order landscapes for a single analog spin triplet, representing a single, unconnected graph vertex. That is, we consider only the terms with prefactor A from Eqs. (3) and

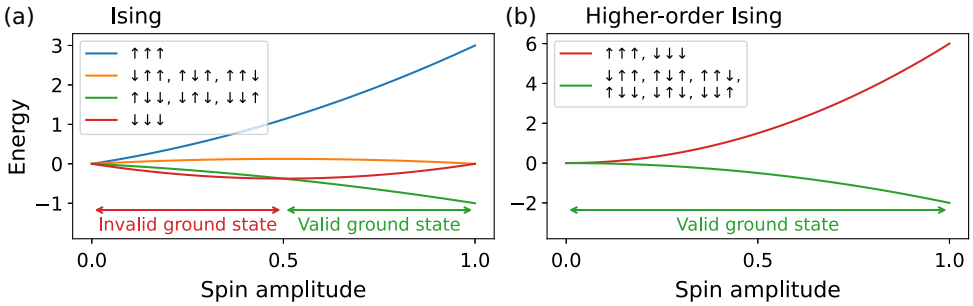

FIG. 2. Energy landscape for a single vertex, represented by a spin triplet, assuming equal spin amplitudes. For the Ising formulation (a), the lowest energy configuration is only correctly one-hot encoded at sufficiently large spin amplitudes. For smaller amplitudes, the ground state (↓↓↓) violates this constraint. In contrast, the higher-order Ising formulation (b) yields a valid ground state for all amplitude values.

(5), and normalize the energy values for direct comparison between the formulations. Figures 1(c) and 1(d) highlight the states with energy below an arbitrary threshold of -0.9, corresponding to the allowed spin configurations defined in Eqs. (4) and (6), respectively. In the Ising landscape [Fig. 1(c)], the allowed configurations are separated by energy barriers, resulting in a rugged energy landscape. In contrast, the higher-order Ising landscape [Fig. 1(d)] features a barrier-free path connecting the allowed states. Similar to the case of discrete spins, the higher-order formulation allows analog spins to access a larger portion of the configuration space, where transitions between allowed states can occur without overcoming energy barriers.

It is well known that amplitude inhomogeneity can reduce the performance of analog solvers, such as analog IMs, since it may lead to an improper mapping of the COPs they aim to solve [37]. To counteract this, many of these solvers include mechanisms specifically aimed at suppressing such inhomogeneities [17,25]. With this in mind, we consider paths for which the three spins have equal amplitudes (i.e., $(\pm s, \pm s, \pm s)$, for all $s \in [0, 1]$). In Fig. 1, these paths extend from the origin to the corners of the cube. Figure 2(a) shows the Ising energy of Eq. (3) along these paths. For large spin amplitudes ($s > 0.5$), we observe the desired behavior: the three valid one-hot encoded states of Eq. (4) are energetically degenerate, and they are lower in energy than the invalid configurations. At lower amplitudes ($s < 0.5$), however, the ↓↓↓ configuration, which violates the one-hot encoding constraint, is the ground state. This arises from the scaling mismatch between the linear and quadratic terms in Eq. (3), which makes the linear terms dominate over the quadratic terms for small spin amplitudes. Since these linear terms are positive, the energy is minimized by pointing the spins down. This presents a challenge because many analog solvers initialize spin amplitudes near zero [14,15,17,38]. As a result, the system may initially favor the incorrect ↓↓↓ configuration, which can act as a distractor during solver operation. As shown in more detail in our recent work [35], such imbalances can indeed degrade performance if not properly mitigated in the solver's dynamics. Figure 2(b) shows the higher-order Ising energy of Eq. (5) along the paths of equal spin amplitudes. In contrast to the Ising formulation, we observe that the valid states of Eq. (6) are energetically favorable for all values of the spin amplitude s. In other words, we observe no imbalances for the higher-order Ising formulation, which results from the fact that the suppression of invalid states (↑↑↑ and ↓↓↓) is performed with quadratic terms only.

We now extend our discussion to the case of two connected vertices, each represented by a spin triplet. In Fig. 3(a), we visualize the lowest-energy spin configurations of the Ising formulation, under the assumption of homogeneous spin amplitudes, and for $B/A = 1$. The green curve corresponds to a correct one-hot encoding for both triplets, with the vertices assigned different colors, thus solving the max-3-cut problem. However, as in Fig. 2(a), this configuration only becomes energetically favorable at sufficiently large spin amplitudes ($s > 0.6$). For smaller amplitudes ($s < 0.6$), it is favorable to set both triplets to the invalid ↓↓↓ state. As shown in Appendix D, this behavior persists for other values of B/A, with the transition between ground states occurring at different values of s. As discussed before, this preference for ↓↓↓ triplets at small amplitudes results from the linear terms outweighing the quadratic terms in the Ising formulation of Eq. (3) at small spin amplitudes.

One might expect a similar issue in the higher-order Ising formulation of Eq. (5), where the quadratic terms could dominate the fourth-order ones at small amplitudes. However, Fig. 3(b) shows that the max-3-cut solution (green curve) remains the ground state across all values of s. In Appendix D, we further show that this holds for any value of $B/A > 0$. While this observation is limited to the case of two connected vertices, the underlying structure of Eq. (5) offers insight into its broader potential. The quadratic and fourth-order terms play different roles: the former enforces one-hot encoding (scaled by A),

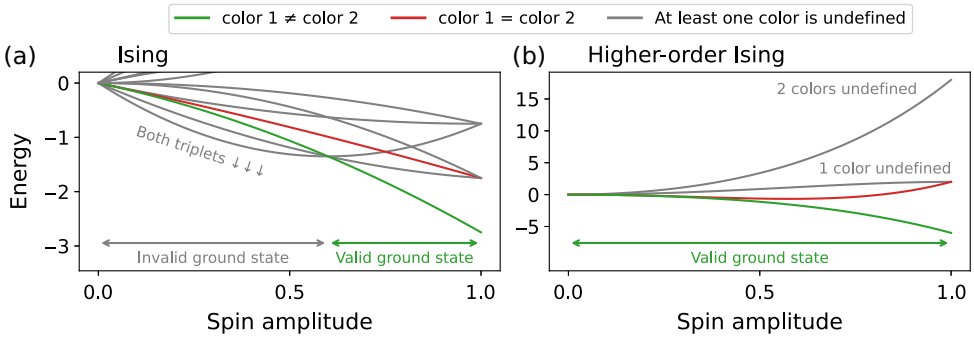

FIG. 3. Energy landscape for two connected vertices, assuming equal spin amplitudes. (a) For the Ising formulation, the lowest energy configuration corresponds to a correct max-3-cut solution (green) only at sufficiently large spin amplitudes. For smaller amplitudes, the ground state is ↓↓↓ for both vertices, violating the one-hot encoding constraint. (b) For the higher-order Ising formulation, the ground state solves the problem regardless of the value of the spin amplitude. In both cases, $B/A = 1$ is used. In Appendix D, we show that different values of B/A yield similar energy landscapes.

while the latter promotes the max-3-cut objective (scaled by B). Hence, any imbalance in the relative strength of the quadratic and fourth-order terms essentially modifies the effective value of B/A. Since B/A is a hyperparameter, optimizing its value can partly compensate for these imbalances. In contrast, for the Ising formulation of Eq. (3), both the one-hot encoding constraint and the max-3-cut objective are enforced using a combination of linear and quadratic terms. Because the linear terms are strictly positive, imbalances distort the energy landscape more drastically, making the ↓↓↓ configuration energetically favorable even though it violates the intended encoding.

IV. PERFORMANCE COMPARISON OF THE FORMULATIONS

In this section, we compare the performance of the max-3-cut formulations introduced in Sec. II across several graph instances. The first set consists of Erdös-Rényi graphs generated according to the $G(n,p)$ model with edge probability $p = 0.5$. For each number of vertices $n \in \{5, 10, 20, 30, 40, 50\}$, we generate 10 instances. We additionally include 10 graphs with 60 vertices from the Biq Mac g05 benchmark set [39], which follows a similar Erdös-Rényi $G(n,m)$ model. Optimal solutions for these instances are computed using the publicly available `max_k_cut` solver [40]. Following the same Erdös-Rényi $G(n,m)$ model, we further evaluate the first five instances from the Gset benchmark set [41], each containing 800 vertices. For these graphs, we use the best known solutions reported in Ref. [42]. All problem definitions, solutions, and a code implementation of the benchmarking study described below are available in Ref. [43].

The formulations are mapped onto an analog IM that is designed to find the minimal energy configuration of the following higher-order Ising Hamiltonian:

$$\mathcal{H} = -\sum_{i}^{N} J_i^{(1)}\sigma_i - \sum_{i<j}^{N} J_{ij}^{(2)}\sigma_i\sigma_j - \sum_{i<j<k<l}^{N} J_{ijkl}^{(4)}\sigma_i\sigma_j\sigma_k\sigma_l. \tag{8}$$

Here, N is the total number of spins. Since each vertex $v \in V$ is encoded using three spins, we have $N = 3|V|$. The coefficients $J^{(p)}_{i_1\ldots i_p}$ denote real-valued interaction strengths of order p and depend on both the chosen formulation and the graph (explicit expressions are provided in Appendix B).

The temporal evolution of spin s_i in the IM is governed by

$$\frac{ds_i}{dt} = -s_i + \tanh\left(\alpha s_i + \beta I_i\right), \tag{9}$$

where α is the linear gain. β is the interaction strength, which follows a commonly used linear annealing scheme [44,45] (see Appendix A for more details). I_i is the local field of s_i, which is further modeled as

$$I_i = \begin{cases} J_i^{(1)} + \sum_j J_{ij}^{(2)}\ \mathrm{sgn}(s_j), & \text{for Ising,} \\ \sum_j J_{ij}^{(2)}\ \mathrm{sgn}(s_j) \\ \quad + \sum_{j<k<l} J_{ijkl}^{(4)}\ \mathrm{sgn}(s_j s_k s_l), & \text{for higher-order Ising.} \end{cases} \tag{10}$$

Here, $\mathrm{sgn}(\cdot)$ denotes the sign function. We adopt this local field model, which is inspired by the simulated bifurcation algorithm [14,34], because it effectively incorporates interactions of different orders [35,46]. As discussed in the previous section, mixed-order interactions can introduce imbalances that degrade solver performance. The use

of the sign function in Eq. (10) mitigates this issue by ensuring that higher-order and lower-order contributions are treated consistently, preventing any one interaction order from disproportionately dominating the dynamics. While, for the small-scale problem discussed in the previous section, we demonstrated that such imbalances are more pronounced for the Ising formulation than for higher-order formulation (cf. Figs. 2 and 3), they are also expected to arise in the higher-order case as problem size increases. Hence, we employ the spin sign method for all formulations in the following benchmark.

The IM is simulated by numerically integrating Eqs. (9) and (10) via the Euler-Maruyama method, which includes stochastic noise (see Appendix A for details, and Ref. [43] for the associated code). We compare the formulations of Sec. II in terms of time-to-solution (TTS):

$$\mathrm{TTS} = \begin{cases} T, & \text{if } P > 0.99, \\ T\dfrac{\log(0.01)}{\log(1-P)}, & \text{if } 0 < P \leq 0.99, \\ \infty, & \text{if } P = 0, \end{cases} \tag{11}$$

which denotes the time needed to reach the target state with 99% probability. Here T is the (dimensionless) time window over which Eq. (9) is integrated, and P is the probability of reaching the target solution within that time window. For each problem instance and for each set of hyperparameters (cf. Appendix A), $T \in [0, 10^4]$ is selected to minimize the resulting TTS.

In Fig. 4, we compare the max-3-cut formulations of Sec. II in terms of TTS. Figure 4(a) compares the Ising formulation of Eq. (3) with the higher-order formulation of Eq. (5). The COPs with up to 180 spins reside below the diagonal, in the light blue region, indicating that they are solved faster using the higher-order formulation than using the standard quadratic one. Moreover, the five instances with 2400 spins lie in the gray region on the right, indicating the Ising formulation failed to solve them for all tested hyperparameter values (cf. Appendix A) within the maximum allowed time $t_{\max} = 10^4$, resulting in a success rate of zero and TTS $= \infty$. By contrast, the higher-order formulation did succeed on these larger instances, yielding finite TTS values. This highlights the clear advantage of the higher-order formulation over the original Ising formulation.

A similar picture is obtained in Fig. 4(b), which compares the original Ising formulation with its rescaled variant from Eq. (7). Here, six of the smallest instances favor the unscaled Ising formulation, while the rescaled version performs better on all others. As in Fig. 4(a), the five larger COPs lie in the gray area on the right, underscoring the inferior performance of the original Ising formulation.

Finally, Fig. 4(c) directly compares the higher-order and rescaled Ising formulations. The higher-order formulation solves all instances faster, demonstrating a consistent performance advantage. On average, it is 5.12 ± 3.64 times faster than the rescaled Ising formulation. This trend is corroborated in Fig. 12 of Appendix F, which provides a direct comparison of the three formulations as a function of the problem size.

The strong performance of the higher-order formulation compared to the original Ising formulation, as shown in Fig. 4(a), aligns with expectations: the higher-order formulation leverages a larger part of the configuration space and removes energy barriers between allowed vertex configurations. The benefit of rescaling the Ising formulation,

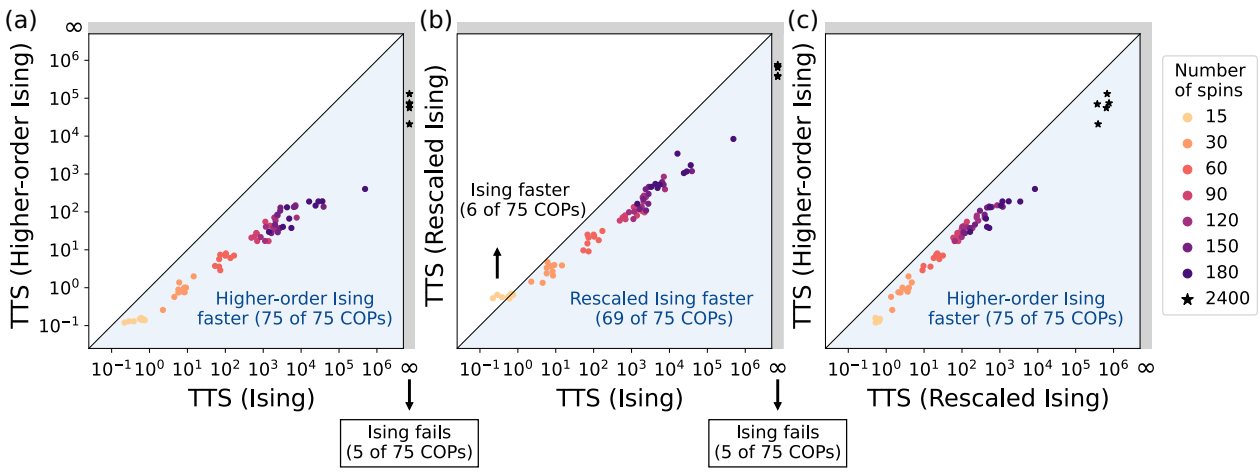

FIG. 4. Comparison of time-to-solution for three max-3-cut formulations [Eqs. (3), (5), and (7)]. Panels (a) and (b) show that both the higher-order Ising formulation and the rescaled Ising formulation outperform the standard Ising formulation. Five COPs with 2400 spins (★) appear in the shaded region on the right, indicating that the standard Ising formulation failed to solve them within the time limit of $t_{\max} = 10^4$. Panel (c) further indicates that the higher-order formulation generally leads to faster solutions than the rescaled quadratic one.

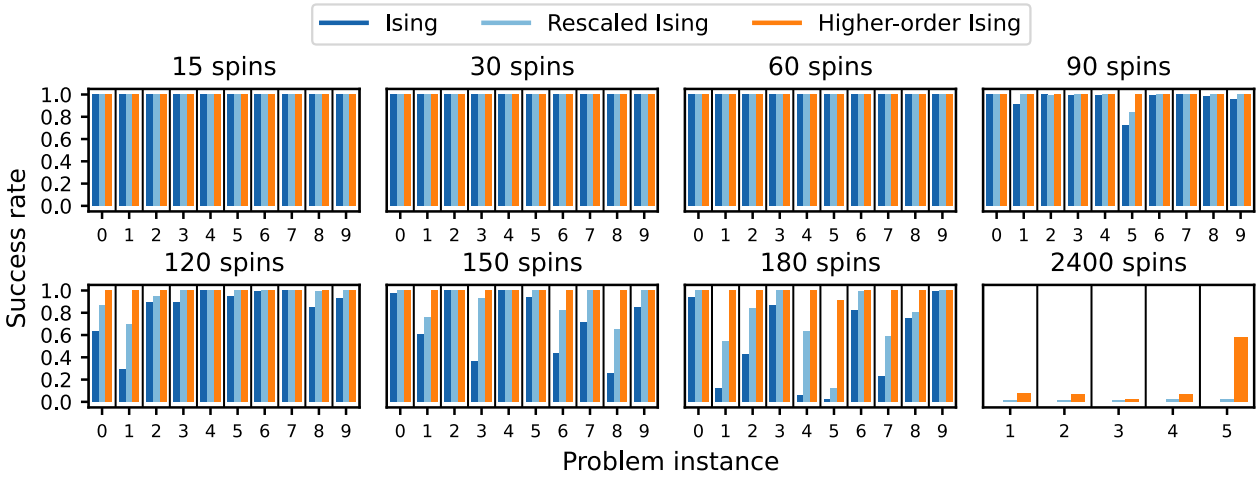

FIG. 5. Comparison of success rates for three max-3-cut formulations [Eqs. (3), (5), and (7)]. Each panel shows instances of a fixed problem size (see panel titles). Instance identifiers are given on the x axis (cf. Ref. [43] for problem definitions). Across all instances, the higher-order formulation achieves success rates that are at least as high as those of the other two formulations (see also Fig. 11).

as illustrated in Fig. 4(b), is consistent with the observations in Refs. [35,36]. Nonetheless, Fig. 4(c) demonstrates that the rescaled Ising formulation is also outperformed by the higher-order approach.

We now validate these conclusions using a second performance metric: the success rate. While Fig. 4 reported the obtained values of $\min_\Theta$ TTS, where Θ denotes the set of hyperparameters (cf. Appendix A), Fig. 5 presents $\max_\Theta$ SR. For instances with fewer than 90 spins, all formulations achieve a 100% success rate. For larger instances, where differences arise, our higher-order formulation performs best, followed by the rescaled Ising formulation, and finally the original Ising formulation. For convenience, Fig. 11 in Appendix E provides a relative comparison of the methods.

V. DISCUSSION

In this work, we introduced a higher-order Ising formulation for the max-3-cut problem. Unlike the commonly used Ising formulation, which relies on one-hot encoding and yields rugged energy landscapes, the higher-order formulation enables smoother landscapes by allowing transitions between valid configurations through single-spin flips. We have shown that this structural advantage extends to the analog setting, where binary variables are relaxed to continuous spins, making the formulation well suited for analog solvers.

Benchmarking on an analog IM confirmed that the higher-order formulation outperforms the standard Ising formulation as well as a rescaled Ising variant that had been proposed in earlier work. The higher-order formulation generally yields higher success rates and shorter time-to-solution. This confirms that the improved structure of the higher-order Ising landscape translates into meaningful performance gains.

These findings illustrate a broader point: while mathematically sound mappings—such as those derived in Ref. [9]—are widely used, they are not necessarily optimal in practice. One way they can be improved is through expanding the design space with higher-order spin interactions, as we have done here. This allowed us to remove some of the energy barriers that were inherent to the Ising formulation of Eq. (3).

Another way is through heuristic rescalings. Indeed, the rescaled version of the Ising formulation we included here [Eq. (7)] outperforms the original formulation. Interestingly, the rescaling has little impact on the energy landscape of the small building blocks that compose the standard Ising formulation. It turns out that its benefits arise only for larger graphs, as can be seen in Fig. 4(b). This points to the importance of empirical tuning. However, relying on manual tuning also raises concerns about scalability and consistency. Building on this, a natural next step is to move beyond manual tuning and toward more systematic data-driven strategies. Recent and ongoing efforts have begun to explore how machine learning might uncover effective mappings from representative COP instances [47,48]. In this light, tailoring formulations to specific problem classes and solver architectures appears to be a promising next step.

Our findings suggest several concrete directions for future work. One direction is to evaluate how the performance of the higher-order and rescaled Ising formulations evolves with increasing problem size and varying graph density. Another is to gain a deeper understanding of the behavior of the rescaled Ising formulation on larger instances, using more advanced tools to visualize its energy landscapes, such as disconnectivity graphs and

basin graphs [22,49]. Such insights could inform further improvements to the higher-order formulation, potentially through a similar rescaling strategy. Finally, it would be valuable to assess whether higher-order formulations similar to those studied here can be extended beyond the uniform three-state Potts model considered in this work, for instance, to state-dependent Potts interactions or a larger number of states. In doing so, it would be valuable to construct alternative formulations using different encoding strategies, such as binary encodings and domain-wall encodings [10].

Overall, our study underscores the interplay between theoretical formulation, energy landscape structure, and empirical solver performance—especially in analog settings—and opens up a broader design space for future combinatorial optimization methods.

ACKNOWLEDGMENTS

This research was funded by the Prometheus Horizon Europe project 101070195. It was also funded by the Research Foundation Flanders (FWO) under grants G028618N,G029519N,G0A6L25N, and G006020N. Additional funding was provided by the EOS project "Photonic Ising Machines". This project (EOS number 40007536) has received funding from the FWO and FRS-FNRS under the Excellence of Science (EOS) program. The work was also partly supported by the Defense Advanced Research Projects Agency (DARPA) under Air Force Research Laboratory (AFRL) contract no. FA8650-23-3-7313. The resources and services used in this work were provided by the VSC (Flemish Supercomputer Center), funded by the Research Foundation—Flanders (FWO) and the Flemish Government.

R.D.P. performed the simulations and wrote the manuscript. G.V.d.S., P.B., and T.V.V. supervised the project. All authors discussed the results and reviewed the manuscript.

DATA AVAILABILITY

The data that support the findings of this article are openly available [43].

APPENDIX A: SIMULATION OF THE ANALOG ISING MACHINE

This appendix describes the simulation methods used to obtain Figs. 4 and 5. The corresponding code is available in Ref. [43]. As detailed in Sec. IV, the temporal evolution of the analog IM is governed by Eqs. (9) and (10). These equations are integrated via the Euler-Maruyama method:

$$\mathbf{s}_{t+1} = \mathbf{s}_t + \Delta t\,(-\mathbf{s}_t + \tanh(\alpha \mathbf{s}_t + \beta_t \mathbf{I}_t)) + \gamma \boldsymbol{\xi}_t, \quad \text{(A1)}$$

where $\mathbf{s}_t$ denotes the vector of spin amplitudes at time t, $\Delta t = 0.01$ is the time step, α is the linear gain, $\gamma = 0.001$ is the noise strength and $\boldsymbol{\xi}_t$ is a vector of real values that are randomly drawn from a Gaussian distribution with mean zero and standard deviation $\sqrt{\Delta t} = 0.1$. $\mathbf{I}_t$ is the vector of local fields, as defined in Eq. (10). β_t is the interaction strength, which follows a commonly used linear annealing scheme [44,45]:

$$\beta_{t+1} = \beta_t + v_\beta \Delta t, \quad \text{(A2)}$$

where v_β is the annealing speed and $\beta_0 = 0$. The iterative updates of Eqs. (A1) and (A2) proceed until the IM obtains the ground-state energy or, alternatively, until it completes $10^4/\Delta t$ steps (whichever comes first).

For each formulation (defined in Sec. II) and for each problem instance, we conduct a grid search over the hyperparameters listed below. For each hyperparameter configuration, the IM evolution is repeated 100 times to estimate the success rate and the TTS [as defined in Eq. (11)]. The values shown in Fig. 4 correspond to the configurations with the lowest TTS, while Fig. 5 shows the configurations with the highest success rates.

We scan the linear gain α and the annealing speed v_β over the following values:

- $\alpha \in \{-10, -7.25, -4.5, -1.75, 1\}$.
- $v_\beta \in \{10^{-4}, 10^{-3}, 10^{-2}, 10^{-1}\}$.

The ratio B/A is scanned linearly from zero to a formulation-dependent upper bound. Since the energy landscapes of Eqs. (3), (5), and (7) are only influenced by the ratio of A and B, we set $A = 1$ during simulation.

For the instances with up to $N = 180$ spins, the following ranges are used:

- $[0, 45/N - 0.1]$, for the original Ising formulation;
- $[0, 180/N]$, for the rescaled Ising formulation;
- $[0, 39/N - 0.1]$, for the higher-order formulation.

For the instances with $N = 2400$ spins, custom ranges are used:

- $[0.01, 0.25]$, for the original Ising formulation;
- $[0.13, 0.27]$, for the rescaled Ising formulation;
- $[0, 0.07]$, for the higher-order formulation.

For each formulation and each problem size, Fig. 6 presents the median TTS value (across the corresponding instances) as a function of B/A. In every panel, the median TTS value reaches a minimum at a specific value of B/A, which confirms that the selected ranges cover the relevant region.

Note that the two leftmost panels in the top row (original Ising formulation with 15 and 30 spins) display bars at B/A

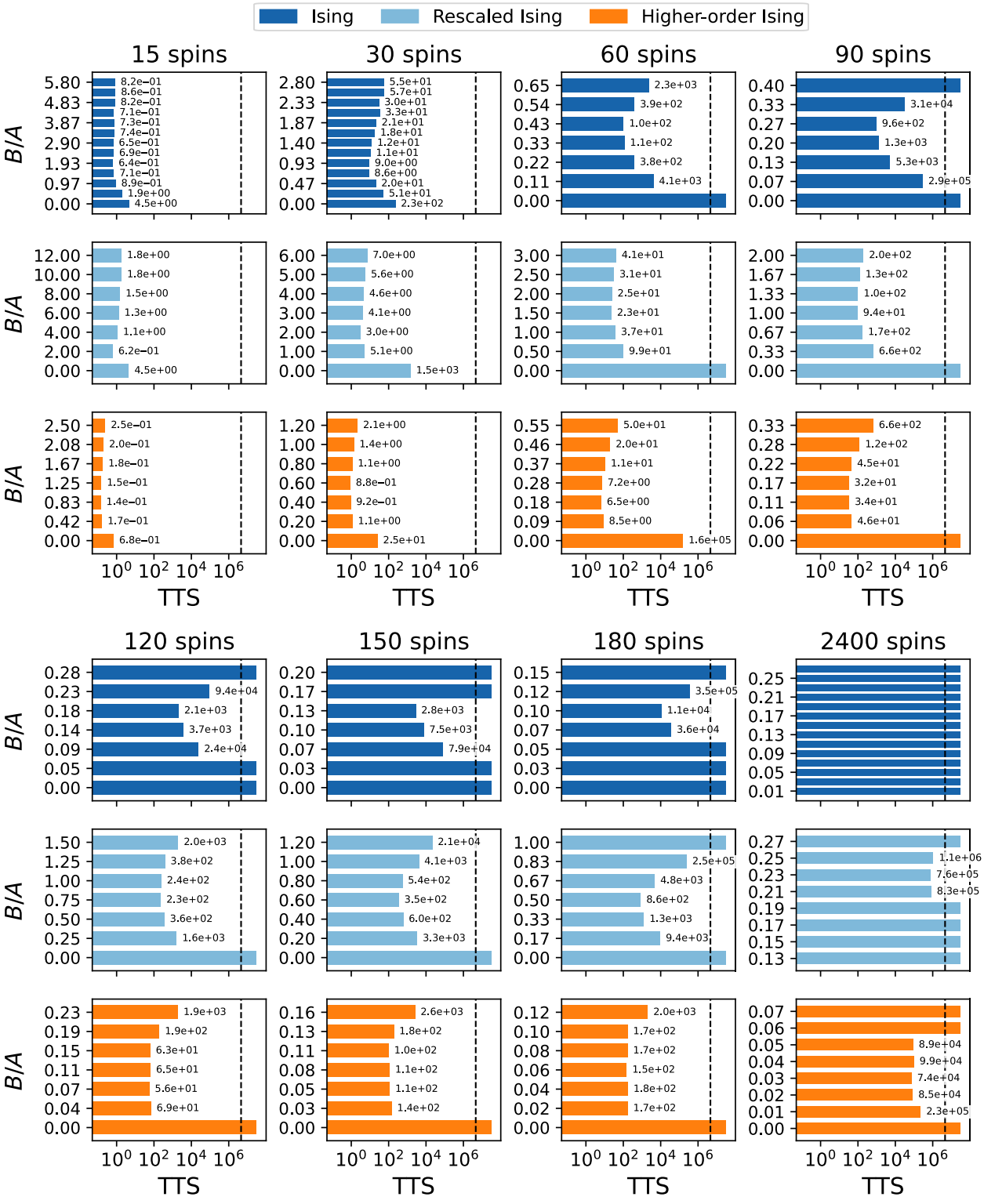

FIG. 6. Validation of mapping parameters B/A. Rows 1–3 respectively show the median time-to-solution (TTS) of the Ising (dark blue), rescaled Ising (light blue), and higher-order (orange) formulations for COP instances of 15–90 spins (see panel titles). Rows 4–6 show instances with 120–2400 spins. Each bar corresponds to a specific value of B/A (y axis) and reports the median TTS across all instances of equal size. The dashed line marks the resolution limit, $t_{\max}\log(0.01)/\log(1-1/N_{\text{repeat}}) = 10^4\log(0.01)/\log(0.99) = 4.6\cdot 10^6$ [cf. Eq. (11)]. Across all formulations and problem sizes, the TTS reaches a minimum with the scanned B/A range, validating the chosen ranges.

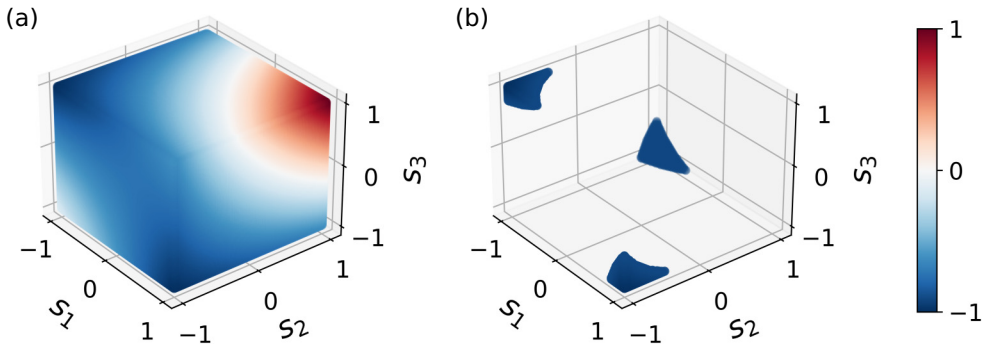

FIG. 7. Normalized energy landscapes for a single vertex, represented by a spin triplet, under the rescaled Ising formulation of Eq. (7). Panel (b) highlights states with energy below –0.9. These figures look similar to Figs. 1(a) and 1(c), indicating that the rescaled Ising formulation and the standard Ising formulation behave similarly for this small problem.

values beyond the nominal upper bound of $45/N - 0.1$. These extra B/A values are included solely to aid the visual check in Fig. 6 and do not affect the results shown in Fig. 4. Indeed, the optimal B/A values remain below $45/N - 0.1$, and the corresponding optimal TTS values are unchanged if only the lowest seven B/A values are considered. Also note that for the instances with 2400 spins, all configurations of the original Ising formulation yield zero success rate (i.e., TTS $= \infty$).

APPENDIX B: EXPLICIT EXPRESSIONS FOR ISING INTERACTION STRENGTHS $J^{(p)}_{i_1 \ldots i_p}$

In this section, we provide explicit expressions for the Ising coefficients $J^{(p)}_{i_1 \ldots i_p}$ in Eq. (8) for each of the max-3-cut formulations under consideration.

Whereas the formulations of Eqs. (3), (5), and (7) employ spin variables that are indexed as $\sigma_{v,c}$ where $v \in V$ is a vertex and $c \in \{1, 2, 3\}$ is a color index, here we instead adopt the flattened single-index notation σ_i, where $i \in \{1, \ldots, 3|V|\}$. The mapping between both indexings is given by

$$i = (c - 1)|V| + v, \tag{B1}$$

such that each spin index i uniquely identifies a vertex–color pair through

$$v(i) = ((i - 1) \mod |V|) + 1, \tag{B2}$$

$$c(i) = \left\lfloor \frac{i - 1}{|V|} \right\rfloor + 1. \tag{B3}$$

1. (Rescaled) Ising formulation

The linear and quadratic interaction coefficients for the max-3-cut Ising formulations of Eqs. (3) and (7) take the following forms (where $\zeta = 1$ and $\zeta = 0.6$, respectively):

$$J^{(1)}_i = -\zeta \left(\frac{A}{2} + \frac{B}{4} \deg\left(v(i)\right) \right), \tag{B4}$$

$$J^{(2)}_{ij} = -\frac{A}{4} \delta_{v(i),v(j)} \left(1 - \delta_{c(i),c(j)}\right) - \frac{B}{4} C_{v(i),v(j)} \delta_{c(i),c(j)}, \tag{B5}$$

where $\deg(v)$ denotes the degree of vertex v and $\mathbf{C}$ is a connectivity matrix in which $C_{uv} = 1$ if vertices u and v are connected, and 0 otherwise. The code implementation of this mapping is provided via Ref. [43].

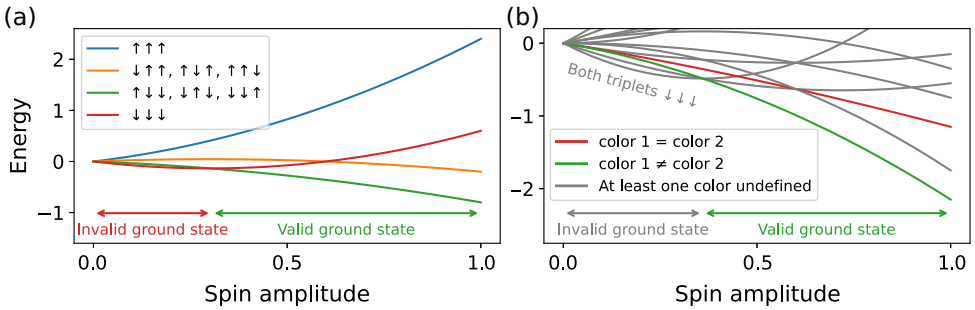

FIG. 8. Energy landscapes of the rescaled Ising formulation for (a) a single vertex, and (b) two connected vertices. We assume homogeneous spin amplitudes. For (b), $B/A = 1$ is used. These figures look similar to Figs. 2(a) and 3(a), indicating that the rescaled Ising formulation and the standard Ising formulation behave similarly for this small problem.

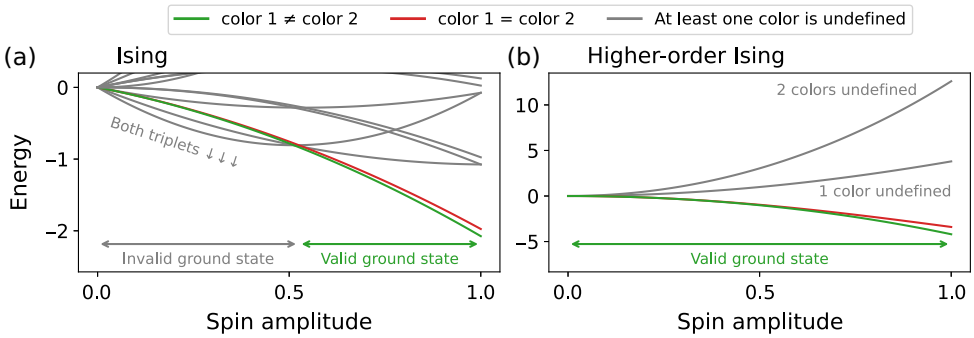

FIG. 9. Energy landscape for two connected vertices, assuming equal spin amplitudes. In contrast to Fig. 3, this figure uses a value of $B/A = 0.1$ for both formulations.

2. Higher-order Ising formulation

The quadratic and quartic interaction coefficients for the higher-order max-3-cut formulation of Eq. (5) take the following forms:

$$J_{ij}^{(2)} = -A\,\delta_{v(i),v(j)}\left(1-\delta_{c(i),c(j)}\right), \tag{B6}$$

$$J_{ijkl}^{(4)} = -B\,C_{v(i),v(j)}\,\delta_{v(i),v(k)}\,\delta_{v(j),v(l)} \cdot \delta_{c(i),c(j)}\,\delta_{c(k),c(l)}\left(1-\delta_{c(i),c(k)}\right). \tag{B7}$$

The code implementation of this mapping is provided via Ref. [43].

APPENDIX C: ANALOG ENERGY LANDSCAPES FOR THE RESCALED ISING FORMULATION

The energy landscape visualizations for small graphs in Sec. III include both the standard Ising formulation of Eq. (3) and the higher-order Ising formulation of Eq. (5). Here, we focus on the rescaled Ising formulation defined in Eq. (7) and demonstrate that it yields energy landscapes similar to those of the standard Ising mapping for these graphs. This observation is consistent with the performance trends shown in Fig. 4(b), where the empirical rescaling only begins to affect performance as the problem size increases further.

Figure 7 shows the energy landscape of a single spin triplet under the rescaled Ising formulation. The result closely resembles Figs. 1(a) and 1(c), indicating minimal qualitative differences between the two Ising variants at this scale. Also for the rescaled Ising formulation, Fig. 8 shows the energy landscapes for a single vertex [Fig. 8(a)] and two connected vertices [Fig. 8(b)] under the assumption of homogeneous spin amplitudes. Comparison with Figs. 2(a) and 3(a) shows that the energy landscapes of both quadratic Ising variants are similar. The differences between the standard Ising formulation and the rescaled Ising variant can be understood as follows. First note that the linear terms in Eq. (3) are all strictly positive. This means that these terms make it more energetically favorable for the spins to be in a down state. Going from Eqs. (3) to (7), the empirical rescaling weakens these linear terms by a factor of 0.6. Hence, down states are somewhat destabilized, and we observe in Fig. 8(a) that the $\downarrow\downarrow\downarrow$ configuration (red curve) is destabilized with respect to its position in Fig. 2(a). Similarly, in Fig. 8(b) we see that the curve with two $\downarrow\downarrow\downarrow$ configurations is destabilized with respect to Fig. 3(a).

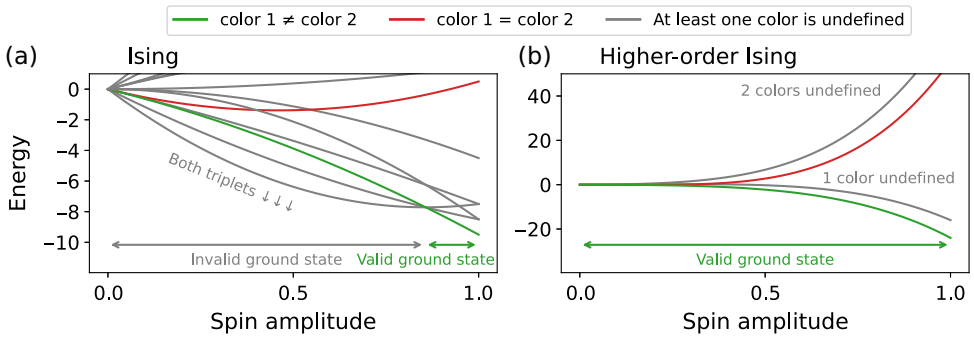

FIG. 10. Energy landscape for two connected vertices, assuming equal spin amplitudes. In contrast to Fig. 3, this figure uses a value of $B/A = 10$ for both formulations.

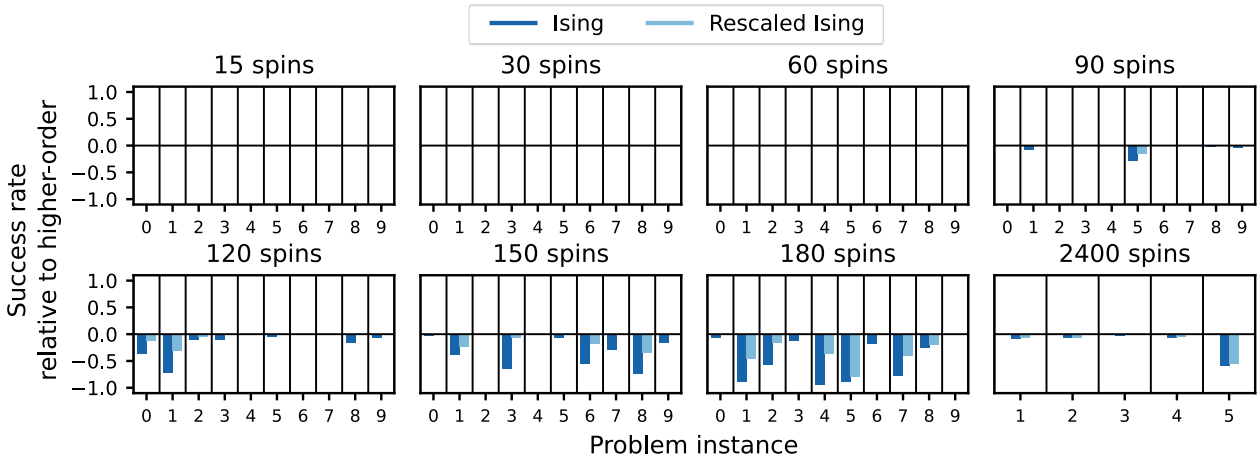

FIG. 11. Success rates obtained by the quadratic Ising formulations [Eqs. (3) and (7)], relative to the higher-order formulation [Eq. (5)]. Instance identifiers are given on the x axis (see Ref. [43] for problem definitions). All relative success rates are negative, indicating that the higher-order formulation achieves success rates that are at least as high as those of the other two formulations.

APPENDIX D: ENERGY LANDSCAPE FOR TWO CONNECTED NODES WHILE VARYING B/A

Figure 3 in the main text shows the energy landscape under the Ising formulation of Eq. (3) and the higher-order Ising formulation of Eq. (5) while assuming equal spin amplitudes. Moreover, this figure employs a value of $B/A = 1$. Here we demonstrate how this figure changes when we vary B/A. Figures 9 and 10 visualize the landscape for $B/A = 0.1$ and $B/A = 10$, respectively.

For the Ising formulation [Figs. 9(a) and 10(a)], we observe that under the new values of B/A, the same ground states remain present: for small spin amplitudes, the ground state is $\downarrow\downarrow\downarrow$ for both triplets, while for larger amplitudes, the max-3-cut solution (green line) is the ground state. However, the value of the spin amplitude where the ground state switches depends on B/A: larger values of B/A shift the switching point to the right, leading to a larger region of incorrect ground state.

For the higher-order Ising formulation [Fig. 9(b) and Fig. 10(b)], the ground state corresponds to the max-3-cut solution, independent of the value of the spin amplitude. We now prove that this holds for any value of $B/A > 0$ under the assumption of homogeneous amplitudes. By substituting all possible spin configurations $(\pm s, \pm s, \pm s)$, for all $s \in [0, 1]$, in Eq. (5), we end up with the following

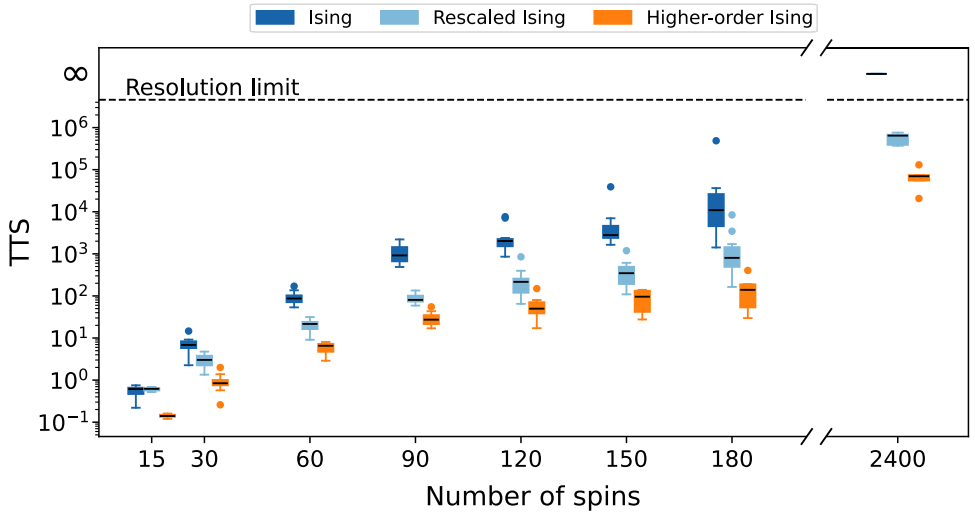

FIG. 12. Time-to-solution for the three max-3-cut formulations [Eqs. (3), (5), and (7)] as a function of problem size. Each boxplot visualizes the distribution of instances of equal size (indicated on the x axis). The dashed line marks the resolution limit, $t_{\max} \log(0.01)/\log(1-1/N_{\text{repeat}}) = 10^4 \log(0.01)/\log(0.99) = 4.6 \cdot 10^6$ (cf. Eq. (11)). The higher-order formulation achieves the fastest solutions overall, followed by the rescaled Ising formulation and then the original Ising formulation.

energies:

$$\mathcal{H} = \begin{cases} -4As^2 - 2Bs^4, & \text{if color 1} \neq \text{color 2}, \\ -4As^2 + 6Bs^4, & \text{if color 1} = \text{color 2}, \\ 4As^2 - 2Bs^4, & \text{if one color is undefined}, \\ 12As^2 + 6Bs^4, & \text{if both colors are undefined}. \end{cases} \tag{D1}$$

It is easy to see that the first case in Eq. (D1), corresponding to the max-3-cut solution where the two vertices have different colors, yields the lowest energy for all $s \in [0, 1]$ and all $B/A > 0$.

APPENDIX E: SUCCESS RATE IMPROVEMENTS OF THE HIGHER-ORDER FORMULATION

Whereas Fig. 5 in the main text shows the absolute success rates obtained by the max-3-cut formulations, Fig. 11 visualizes the success rates of the quadratic Ising formulations [Eqs. (3) and (7)], relative to the higher-order formulation [Eq. (5)]. We observe that the higher-order formulation achieves equal or better success rates for every instance tested.

APPENDIX F: TIME-TO-SOLUTION AS A FUNCTION OF PROBLEM SIZE

Figure 4 in the main text compared the obtained TTS values of the three formulations on a pairwise basis. By contrast, Fig. 12 visualizes the three formulations simultaneously as a function of the problem size. The higher-order formulation consistently achieves the shortest TTS across the full range of instance sizes, demonstrating its advantage in solution efficiency. The rescaled Ising formulation generally performs better than the original Ising reduction.

[1] F. Barahona, M. Grötschel, M. Jünger, and G. Reinelt, An application of combinatorial optimization to statistical physics and circuit layout design, Oper. Res. **36**, 493 (1988).

[2] C. De Simone, M. Diehl, M. Jünger, P. Mutzel, G. Reinelt, and G. Rinaldi, Exact ground states of Ising spin glasses: New experimental results with a branch-and-cut algorithm, J. Stat. Phys. **80**, 487 (1995).

[3] A. Perdomo, C. Truncik, I. Tubert-Brohman, G. Rose, and A. Aspuru-Guzik, Construction of model Hamiltonians for adiabatic quantum computation and its application to finding low-energy conformations of lattice protein models, Phys. Rev. A **78**, 012320 (2008).

[4] R. Y. Li, R. Di Felice, R. Rohs, and D. A. Lidar, Quantum annealing versus classical machine learning applied to a simplified computational biology problem, npj Quantum Inf. **4**, 14 (2018).

[5] C. Hojny, I. Joormann, H. Lüthen, and M. Schmidt, Mixed-integer programming techniques for the connected max-k-cut problem, Math. Program. Comput. **13**, 75 (2021).

[6] J. Poland and T. Zeugmann, in *International Conference on Discovery Science* (Springer, Berlin, Heidelberg, 2006), p. 197.

[7] E. G. Rieffel, D. Venturelli, B. O'Gorman, M. B. Do, E. M. Prystay, and V. N. Smelyanskiy, A case study in programming a quantum annealer for hard operational planning problems, Quantum Inf. Process. **14**, 1 (2015).

[8] R. Carlson and G. L. Nemhauser, Scheduling to minimize interaction cost, Oper. Res. **14**, 52 (1966).

[9] A. Lucas, Ising formulations of many NP problems, Front. Phys. **2**, 74887 (2014).

[10] F. Dominguez, J. Unger, M. Traube, B. Mant, C. Ertler, and W. Lechner, Encoding-independent optimization problem formulation for quantum computing, Front. Quantum Sci. Technol. **2**, 1229471 (2023).

[11] M. Honari-Latifpour and M.-A. Miri, Optical Potts machine through networks of three-photon down-conversion oscillators, Nanophotonics **9**, 4199 (2020).

[12] K. P. Kalinin and N. G. Berloff, Simulating Ising and n-state planar Potts models and external fields with nonequilibrium condensates, Phys. Rev. Lett. **121**, 235302 (2018).

[13] N. Mohseni, P. L. McMahon, and T. Byrnes, Ising machines as hardware solvers of combinatorial optimization problems, Nat. Rev. Phys. **4**, 363 (2022).

[14] H. Goto, K. Endo, M. Suzuki, Y. Sakai, T. Kanao, Y. Hamakawa, R. Hidaka, M. Yamasaki, and K. Tatsumura, High-performance combinatorial optimization based on classical mechanics, Sci. Adv. **7**, eabe7953 (2021).

[15] T. Inagaki, Y. Haribara, K. Igarashi, T. Sonobe, S. Tamate, T. Honjo, A. Marandi, P. L. McMahon, T. Umeki, K. Enbutsu, *et al.*, A coherent Ising machine for 2000-node optimization problems, Science **354**, 603 (2016).

[16] G. Pedretti, F. Böhm, T. Bhattacharya, A. Heittmann, X. Zhang, M. Hizzani, G. Hutchinson, D. Kwon, J. Moon, E. Valiante, *et al.*, Solving Boolean satisfiability problems with resistive content addressable memories, npj Unconv. Comput. **2**, 7 (2025).

[17] T. Leleu, Y. Yamamoto, P. L. McMahon, and K. Aihara, Destabilization of local minima in analog spin systems by correction of amplitude heterogeneity, Phys. Rev. Lett. **122**, 040607 (2019).

[18] E. Farhi, J. Goldstone, S. Gutmann, and M. Sipser, Quantum computation by adiabatic evolution, arXiv:quant-ph/0001106.

[19] E. Farhi, J. Goldstone, and S. Gutmann, A quantum approximate optimization algorithm, arXiv:1411.4028.

[20] S. Hadfield, Z. Wang, B. O'gorman, E. G. Rieffel, D. Venturelli, and R. Biswas, From the quantum approximate optimization algorithm to a quantum alternating operator ansatz, Algorithms **12**, 34 (2019).

[21] R. M. Karp, in *50 Years of Integer Programming 1958–2008: from the Early Years to the State-of-the-Art* (Springer, Berlin, Heidelberg, 2009), p. 219.

[22] D. Dobrynin, A. Renaudineau, M. Hizzani, D. Strukov, M. Mohseni, and J. P. Strachan, Energy landscapes of combinatorial optimization in Ising machines, Phys. Rev. E **110**, 045308 (2024).

[23] M. Hizzani, A. Heittmann, G. Hutchinson, D. Dobrynin, T. Van Vaerenbergh, T. Bhattacharya, A. Renaudineau, D. Strukov, and J. P. Strachan, in *2024 IEEE International*

Symposium on Circuits and Systems (ISCAS) (IEEE, 2024), p. 1.

[24] E. Valiante, M. Hernandez, A. Barzegar, and H. G. Katzgraber, Computational overhead of locality reduction in binary optimization problems, Comput. Phys. Commun. **269**, 108102 (2021).

[25] F. Böhm, T. V. Vaerenbergh, G. Verschaffelt, and G. Van der Sande, Order-of-magnitude differences in computational performance of analog Ising machines induced by the choice of nonlinearity, Commun. Phys. **4**, 149 (2021).

[26] N. G. Berloff, M. Silva, K. Kalinin, A. Askitopoulos, J. D. Töpfer, P. Cilibrizzi, W. Langbein, and P. G. Lagoudakis, Realizing the classical *XY* Hamiltonian in polariton simulators, Nat. Mater. **16**, 1120 (2017).

[27] A. D. King, W. Bernoudy, J. King, A. J. Berkley, and T. Lanting, Emulating the coherent Ising machine with a mean-field algorithm, arXiv:1806.08422.

[28] M. Ercsey-Ravasz and Z. Toroczkai, Optimization hardness as transient chaos in an analog approach to constraint satisfaction, Nat. Phys. **7**, 966 (2011).

[29] H. Goto, K. Tatsumura, and A. R. Dixon, Combinatorial optimization by simulating adiabatic bifurcations in nonlinear Hamiltonian systems, Sci. Adv. **5**, eaav2372 (2019).

[30] S. K. Vadlamani, T. P. Xiao, and E. Yablonovitch, Physics successfully implements lagrange multiplier optimization, Proc. Natl. Acad. Sci. **117**, 26639 (2020).

[31] S. Reifenstein, T. Leleu, T. McKenna, M. Jankowski, M.-G. Suh, E. Ng, F. Khoyratee, Z. Toroczkai, and Y. Yamamoto, Coherent SAT solvers: A tutorial, Adv. Opt. Photonics **15**, 385 (2023).

[32] M. Calvanese Strinati and C. Conti, Multidimensional hyperspin machine, Nat. Commun. **13**, 7248 (2022).

[33] M. Calvanese Strinati and C. Conti, Equalized hyperspin machine, Phys. Rev. A **112**, 053505 (2025).

[34] T. Kanao and H. Goto, Simulated bifurcation for higher-order cost functions, Appl. Phys. Express **16**, 014501 (2022).

[35] R. De Prins, J. Lamers, P. Bienstman, G. Van der Sande, G. Verschaffelt, and T. Van Vaerenbergh, Incorporating external fields in analog Ising machines, Commun. Phys. **8**, 482 (2025).

[36] H. Sakaguchi, K. Ogata, T. Isomura, S. Utsunomiya, Y. Yamamoto, and K. Aihara, Boltzmann sampling by degenerate optical parametric oscillator network for structure-based virtual screening, Entropy **18**, 365 (2016).

[37] T. Leleu, Y. Yamamoto, S. Utsunomiya, and K. Aihara, Combinatorial optimization using dynamical phase transitions in driven-dissipative systems, Phys. Rev. E **95**, 022118 (2017).

[38] A. Yamamura, H. Mabuchi, and S. Ganguli, Geometric landscape annealing as an optimization principle underlying the coherent Ising machine, Phys. Rev. X **14**, 031054 (2024).

[39] A. Wiegele, Biq Mac library—A collection of Max-Cut and quadratic 0-1 programming instances of medium size, https://biqmac.aau.at/biqmaclib.pdf (2007).

[40] R. Fakhimi, and V. Hamidreza, The max k-cut problem on classical and quantum solvers, 2022, https://github.com/qcol-lu/maxkcut

[41] Y. Ye, Gset dataset of random graphs, https://web.stanford.edu/∼yyye/yyye/Gset/ (2003), accessed: 2025-06-19.

[42] F. Ma and J.-K. Hao, A multiple search operator heuristic for the max-*k*-cut problem, Ann. Oper. Res. **248**, 365 (2017).

[43] R. De Prins, Solving Max-3-Cut with an analog Ising machine using multiple formulations, https://github.com/rdprins/Max3CUT_Ising (2025).

[44] A. Yamamura, H. Mabuchi, and S. Ganguli, Geometric landscape annealing as an optimization principle underlying the coherent Ising machine, Phys. Rev. X **14**, 031054 (2024).

[45] J. Lamers, G. Verschaffelt, and G. Van der Sande, Using continuation methods to analyse the difficulty of problems solved by Ising machines, Commun. Phys. **7**, 378 (2024).

[46] R. De Prins, G. Van der Sande, P. Bienstman, and T. Van Vaerenbergh, How to incorporate higher-order interactions in analog Ising machines, arXiv:2507.23621.

[47] F. Richoux and J.-F. Baffier, Automatic error function learning with interpretable compositional networks, Ann. Math. Artif. Intell. **93**, 441 (2023).

[48] F. Richoux, J.-F. Baffier, and P. Codognet, in *International Conference on Computational Science* (Springer, 2023), p. 153.

[49] N. Masuda, S. Islam, S. Thu Aung, and T. Watanabe, Energy landscape analysis based on the Ising model: Tutorial review, PLOS Complex Syst. **2**, e0000039 (2025).